Peptide transporter DtpA has two alternate conformations, one of which is promoted by inhibitor binding

Christian A. Bippes[a], Lin Ge[a], Marcel Meury[b,c], Daniel Harder[b,c], Zöhre Ucurum[b,c], Hannelore Daniel[d], Dimitrios Fotiadis[b,c,1,2], and Daniel J. Müller[a,1,2]

[a]Department of Biosystems Science and Engineering, Eidgenössische Technische Hochschule Zürich, 4058 Basel, Switzerland; [b]Institute of Biochemistry and Molecular Medicine and [c]Swiss National Centre of Competence in Research TransCure, University of Bern, 3012 Bern, Switzerland; and [d]Zentralinstitut für Ernährungs- und Lebensmittelforschung, Research Center of Nutrition and Food Sciences, Technische Universität München, 85350 Freising, Germany

Edited* by H. Ronald Kaback, University of California, Los Angeles, CA, and approved September 4, 2013 (received for review July 9, 2013)

Peptide transporters (PTRs) of the large PTR family facilitate the uptake of di- and tripeptides to provide cells with amino acids for protein synthesis and for metabolic intermediates. Although several PTRs have been structurally and functionally characterized, how drugs modulate peptide transport remains unclear. To obtain insight into this mechanism, we characterize inhibitor binding to the *Escherichia coli* PTR dipeptide and tripeptide permease A (DtpA), which shows substrate specificities similar to its human homolog hPEPT1. After demonstrating that Lys[Z-NO_2]-Val, the strongest inhibitor of hPEPT1, also acts as a high-affinity inhibitor for DtpA, we used single-molecule force spectroscopy to localize the structural segments stabilizing the peptide transporter and investigated which of these structural segments change stability upon inhibitor binding. This characterization was done with DtpA embedded in the lipid membrane and exposed to physiologically relevant conditions. In the unbound state, DtpA adopts two main alternate conformations in which transmembrane α-helix (TMH) 2 is either stabilized (in ~43% of DtpA molecules) or not (in ~57% of DtpA molecules). The two conformations are understood to represent the inward- and outward-facing conformational states of the transporter. With increasing inhibitor concentration, the conformation characterized by a stabilized TMH 2 becomes increasingly prevalent, reaching ~92% at saturation. Our measurements further suggest that Lys[Z-NO_2]-Val interacts with discrete residues in TMH 2 that are important for ligand binding and substrate affinity. These interactions in turn stabilize TMH 2, thereby promoting the inhibited conformation of DtpA.

membrane transporter | proton-dependent oligopeptide transporter | major facilitator superfamily | atomic force microscopy | molecular interactions

The peptide transporter (PTR) family hosts polytopic membrane proteins that occur in all living organisms. They belong to the class of secondary active transporters and use the proton motive force for uptake of di- and tripeptides into cells (1, 2). Therefore, the PTR family also is referred to as the "proton-dependent oligopeptide transporter" (POT) family. This uptake of di- and tripeptides provides cells with amino acids that act as building blocks for protein biosynthesis but also as sources of nitrogen, sulfur, and carbon for the synthesis of various metabolites. During the past years several PTR family transporters have been functionally well characterized (3–12). All these di- and tripeptide transporters share unique specificities (2). On the one hand, they are unspecific, because virtually every possible di- and tripeptide composed of L-amino acids can serve as substrate. On the other hand, the affinity of different peptides to transporters may differ and thus confers each transporter with certain selectivity (2). Peptide transporters also may mediate the translocation of various peptide-like compounds. The mammalian peptide transporters PEPT1 and PEPT2 have been of special interest because they are important for both nutrition and the uptake of orally administered (pro)drugs, e.g., β-lactam antibiotics, the Parkinson's prodrug L-DOPA-Phe, and the antiviral prodrug Val-acyclovir (13, 14).

Sequence analysis of PTR family members reveals that they differ in sequence and size [~450–850 amino acids (aa) in length], but all contain small, highly conserved protein stretches known as "PTR motifs" (1, 15). Mutations in these motifs frequently result in loss of peptide transport (16, 17), indicating the importance of these sequences for the formation of the substrate translocation pathway and the protein–substrate interaction. The PTR family belongs to the structurally and functionally diverse major facilitator superfamily (MFS) whose members contain usually 12 but sometimes 14 transmembrane α-helices (TMHs). For DtpT from *Lactococcus lactis* and human PEPT1 (hPEPT1), 12 TMHs have been verified experimentally (18, 19). The crystal structures of bacterial peptide transporters from *Shewanella oneidensis* ($PepT_{So}$ and $PepT_{So2}$), *Streptococcus thermophilus* ($PepT_{St}$), and *Geobacillus kaustophilus* (GkPOT) revealed 14 TMHs (10, 20–22). In *Escherichia coli*, four PTR family members have been characterized: dipeptide and tripeptide permease A (DtpA, formerly named YdgR or TppB) (3, 4, 23), DtpB (formerly YhiP) (3), DtpC (formerly YjdL) (11, 24–26), and DtpD (formerly YbgH) (27). Among these transporters, DtpA shows peptide selectivity very similar to that of hPEPT1 (3, 4).

Significance

Proton-dependent oligopeptide transporters are attractive candidates for drug research. To understand their functional modulation by drugs, we applied single-molecule force spectroscopy and characterized how peptide transport facilitated by the dipeptide and tripeptide permease A (DtpA) from *Escherichia coli* is inhibited. In the unbound state DtpA embedded in the physiologically relevant membrane adopts two alternate conformations, which differ mainly in whether the transmembrane α-helix TMH2 is stabilized. TMH2 contains residues that are important for ligand binding and substrate affinity. Inhibitor (Lys[Z-NO_2]-Val) binding to DtpA significantly strengthens the interactions stabilizing TMH2 and guides DtpA to populate the inhibited conformation.

Author contributions: C.A.B., D.F., and D.J.M. designed research; C.A.B., L.G., M.M., D.H., and Z.U. performed research; H.D. and D.F. contributed new reagents/analytic tools; C.A.B., L.G., and D.J.M. analyzed data; and C.A.B., D.F., and D.J.M. wrote the paper.

The authors declare no conflict of interest.

*This Direct Submission article had a prearranged editor.

[1]D.F. and D.J.M. share senior authorship.

[2]To whom correspondence may be addressed. E-mail: dimitrios.fotiadis@ibmm.unibe.ch or daniel.mueller@bsse.ethz.ch.

This article contains supporting information online at www.pnas.org/lookup/suppl/doi:10.1073/pnas.1312959110/-/DCSupplemental.

www.pnas.org/cgi/doi/10.1073/pnas.1312959110

These crystal structures and functional studies provided important insight into the working mechanisms of peptide transporters. However, few experimental results helped explain the interactions by which an inhibitor modulates the functional state of PTR family members.

Atomic force microscopy (AFM)-based single-molecule force spectroscopy (SMFS) allows the forces that are generated by inter- and intramolecular interactions of membrane proteins to be quantified and localized (28, 29). SMFS characterizes native membrane proteins at physiologically relevant conditions, including embedding in a lipid bilayer and exposure to buffer solution at ambient temperature. The interaction forces, or simply the "interactions," detected by SMFS can be assigned to structural segments stabilizing the membrane protein. Such stable structural segments can represent single parts or combinations of secondary structural elements such as transmembrane α-helices, β-strands, or polypeptide loops. In the past, SMFS has been used to characterize interactions in membrane proteins induced by ligand or inhibitor binding (30–34), by signal transduction (35), by mutations (36–38), by oligomeric assemblies (39), or by the lipid composition of the bilayer membrane (40). In this work we applied SMFS to localize the interactions that stabilize structural segments of DtpA and to characterize the mechanisms an inhibitor uses to modulate the functional state of the peptide transporter. Therefore, we first investigated the inhibitory effect of the compound Lys[Z-NO_2]-Val, the strongest known inhibitor for hPEPT1 (41, 42), on DtpA by in vivo peptide-uptake experiments. Using SMFS, we then characterized the interaction forces that stabilize DtpA at physiologically relevant conditions in the absence and presence of Lys[Z-NO_2]-Val. This comparative approach allowed us to localize the structural segments stabilizing individual DtpA molecules, to quantify the interaction forces stabilizing each structural segment, and to observe which structural segments of the peptide transporter changed stability upon inhibitor binding. The results show that in the unbound state DtpA has two alternate conformational states, one of which is stabilized by the inhibitor to block peptide transport.

Results

Identifying Lys[Z-NO_2]-Val as an Effective Inhibitor of the Peptide Transporter DtpA. The substrate selectivity of DtpA is very similar to that of its human homolog hPEPT1 (3, 4). Thus, it seems likely that both peptide transporters can be inhibited by the same chemical compound. To investigate this possibility, we used an in vivo uptake assay and determined whether Lys[Z-NO_2]-Val, the strongest known inhibitor of hPEPT1 (41, 42), also affects the activity of DtpA (Fig. 1). The assay, which characterized the uptake of [^{3}H]-Ala-Ala into *E. coli* cells overexpressing DtpA, showed that DtpA was gradually inhibited by increasing concentrations of Lys[Z-NO_2]-Val. The inhibition constant of Lys[Z-NO_2]-Val as revealed by the uptake assay was $K_i = 0.043$ mM. After having found that Lys[Z-NO_2]-Val serves as an effective inhibitor of DtpA, we characterized the interactions that lead to the deactivation of substrate transport by using AFM-based SMFS.

AFM Imaging of Reconstituted DtpA. For SMFS we purified and reconstituted different N- and C-terminally elongated and His-tagged DtpA constructs into dimyristoyl phosphatidylcholine (DMPC) lipid bilayers (*SI Appendix 1*, Table S1 and Fig. S1). The resulting DtpA proteoliposomes (*SI Appendix*, Fig. S2) were adsorbed onto freshly cleaved mica (43) and imaged by contact-mode AFM in buffer solution (Fig. 2*A*). Single-layered membrane patches of varying sizes were found, which suggest that the proteoliposomes opened by adsorption onto mica. At low magnification, the membranes showed two distinct features of different height and roughness. Some areas of the membranes appeared smooth; others appeared rough (Fig. 2*A*). The smooth areas corresponded to lipid void of membrane proteins, with a height of 4.4 ± 0.3 nm ($n = 24$, mean ± SD). The rougher areas had a height of 6.6 ± 0.4 nm ($n = 23$). AFM imaging of the rough area at higher magnification revealed densely packed assemblies and small 2D nanocrystals of DtpA (Fig. 2*B*) in which DtpA molecules were arranged in parallel rows. Repeatedly imaging of the sample showed that the membranes were stable and did not change shape or ultrastructure.

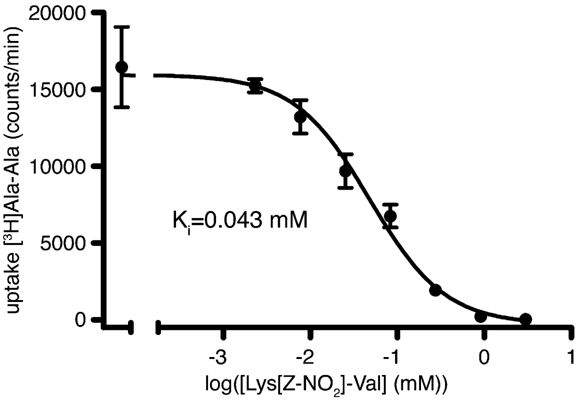

Fig. 1. Lys[Z-NO_2]-Val–dependent peptide uptake by *E. coli* cells overexpressing DtpA. [^{3}H]-Ala-Ala (54 μM, 0.074 Ci/mmol) uptake was inhibited with increasing concentrations of Lys[Z-NO_2]-Val (0, 0.0023, 0.0077, 0.025, 0.083, 0.28, 0.91, and 3 mM). The nonlinear fit yields a K_i of 0.043 mM (95% confidence interval: 0.025–0.075 mM). Data points represent means of triplicates ± SEM. One of two similar experiments is shown.

SMFS of DtpA. We used AFM-based SMFS to detect and quantify the interactions established in DtpA. To do so, we located DtpA-containing membranes by contact-mode AFM imaging (Fig. 2 *A* and *B*). The tip of the AFM cantilever then was pushed onto the membrane with a force of ∼1 nN for 0.5–1 s to facilitate unspecific attachment of the membrane protein to the tip. In ∼0.05% of all attempts ($n \sim 5.5 \times 10^6$), a transporter adhered nonspecifically via one of its terminal ends to the AFM tip (Fig. 2*C*) (28, 44). When the cantilever was retracted from the membrane, the terminal polypeptide was stretched, and a mechanical force was applied to DtpA. At sufficiently high force, a structural segment of the transporter unfolded, and the AFM cantilever relaxed. Further separation of the tip from the membrane stretched the previously unfolded polypeptide and loaded the next structural segment of DtpA with force. Each force peak in a force–distance (F–D) curve (Fig. 2*D*) recorded the unfolding of a structural segment of DtpA and denoted the transition from one unfolding intermediate to the next (28). Thus, DtpA unfolded step by step from the lipid membrane via several unfolding intermediates. The magnitude of each force peak quantified the strength of the inter- and intramolecular interactions that stabilized the corresponding structural segments of DtpA.

Unfolding of Different DtpA Constructs Reveals Specific SMFS Spectra. Using SMFS, we unfolded three different constructs of DtpA by SMFS (Fig. 3 and *SI Appendix*, Fig. S3) that differed in the way the His-tag was engineered to DtpA and in the length of the polypeptide linker connecting the His-tag to the transporter (*SI Appendix*, Table S1). In the first construct, a 20-aa polypeptide containing a His_6-tag was engineered to the N terminus (N-DtpA); in the second, a short, 2-aa peptide and a His_6-tag were attached to the C terminus (C-DtpA); and in the third, a 12-aa polypeptide and a His_{10}-tag were attached to the C terminus (C_{long}-DtpA). Unfolding of N-DtpA resulted in two classes of F–D curves, one of which was predominant, occurring in >90% of cases. Likewise, the unfolding of each of the C-DtpA versions resulted in two classes of F–D curves,

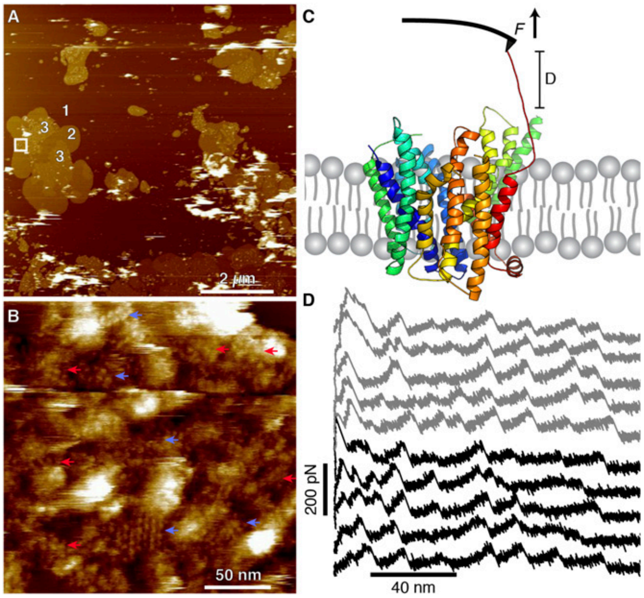

Fig. 2. AFM imaging and SMFS of DtpA reconstituted in DMPC lipid membranes. (*A*) Overview AFM topography of C-DtpA proteoliposomes. Adsorption to mica (marked 1) opened the proteoliposomes, which appeared as single-layered membrane patches. These membranes appeared smooth if composed of lipid only (marked 2) or rough if densely packed with C-DtpA (marked 3). (*B*) Higher-magnification AFM topography of the boxed area in *A*. Red arrows indicate areas of densely packed C-DtpA; blue arrows indicate small areas of C-DtpA organized in 2D nanocrystals. Full color ranges correspond to vertical height scales of 30 nm in *A* and 7 nm in *B*. (*C*) Schematic representation of SMFS on DtpA. The tip of the AFM cantilever picks up one terminus of the membrane-embedded transporter. As the distance, *D*, between the AFM cantilever and the sample surface increases, the polypeptide tethering the tip of the AFM cantilever to DtpA is stretched, and a force, *F*, is applied to the transporter. During this process an F–D curve is recorded. (*D*) Examples of F–D curves corresponding to C-terminal unfolding of C-DtpA (gray curves) and N-terminal unfolding of N-DtpA (black curves). Although every F–D curve shows unique features, all curves share common force peaks at certain tip–sample distances. AFM imaging and SMFS were performed in buffer solution [10 mM Tris-HCl (pH 7.4), 150 mM NaCl] at room temperature. The cartoon in *C* showing the DtpA homolog PepT$_{\mathrm{So}}$ from *S. oneidensis* (Protein Data Bank ID 2XUT) (10) was prepared using PyMol.

one of which occurred in >90% of cases. The predominant force-peak patterns of N-DtpA and C-DtpA are markedly different (Fig. 3). However, the force-peak patterns of the predominant classes of C- and $\mathrm{C_{long}}$-DtpA exhibit the same characteristics (compare Fig. 3*B* and *SI Appendix*, Fig. S3). Comparison of the classes obtained from N-DtpA and $\mathrm{C_{long}}$-DtpA revealed that F–D curves that were rarely detected upon unfolding of $\mathrm{C_{long}}$-DtpA (*SI Appendix*, Fig. S3 *Middle*) had the same force-peak pattern as the F–D curves that were predominantly detected upon unfolding of N-DtpA (*SI Appendix 2* and Fig. S3), and vice versa.

The overall lengths of the force-peak patterns of all F–D curves suggested that the different DtpA constructs were unfolded mechanically into a fully extended conformation (*Methods*), because the unfolded polypeptide can be fully extended only if the protein is attached to the AFM tip by one terminal end and not via any other surface-exposed feature (e.g., a loop connecting TMHs) (28, 44). The two force-peak patterns detected for each DtpA construct indicate that the transporters have been unfolded from the N-terminal end (one pattern) or the C-terminal end (the other pattern) by the pulling of the AFM tip. However, the ratio of these patterns depends on the modification of the DtpA termini (*SI Appendix 3*).

Assigning the SMFS Spectra to the Terminal Unfolding of DtpA. Next, we assigned each of the force-peak patterns (or classes) of F–D curves to the stepwise unfolding of DtpA from either the N-terminal or C-terminal end (*SI Appendix 4*). Therefore, we unfolded the DtpA construct $\mathrm{C_{long}}$-DtpA that carried a much longer artificial C-terminal extension than the C-DtpA construct.

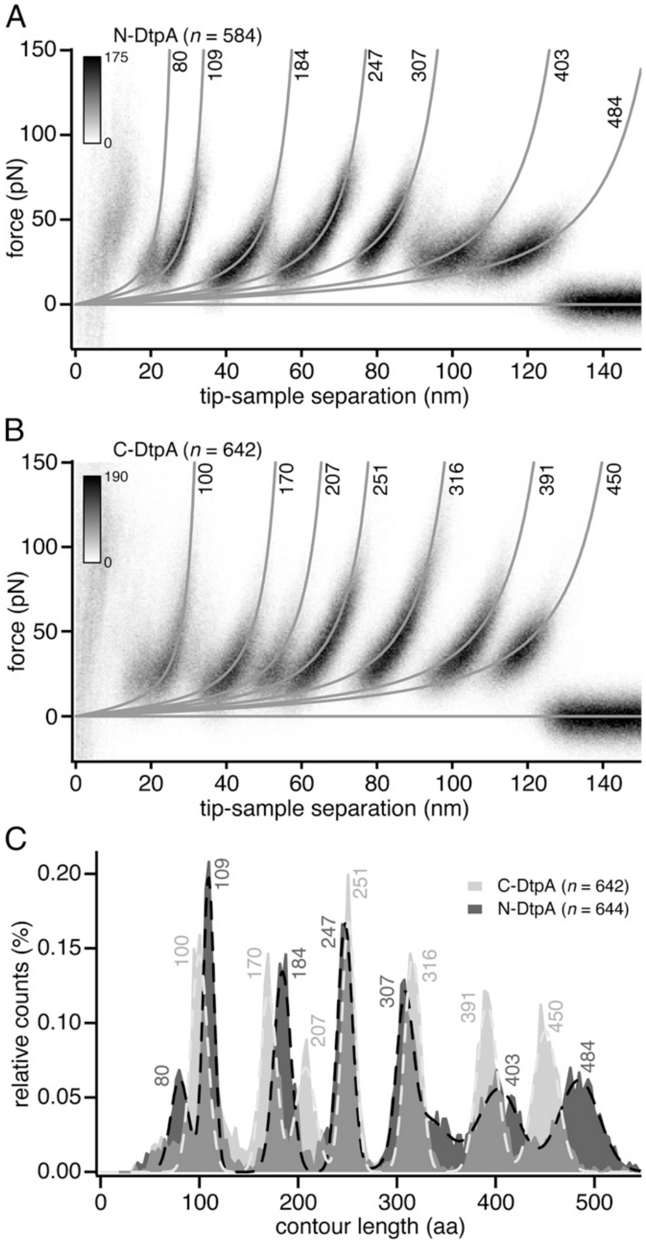

Fig. 3. Predominant unfolding force-peak patterns of N-DtpA and C-DtpA. Density plot representations of superimposed F–D curves corresponding to the predominant classes obtained from N-DtpA (*A*) and C-DtpA (*B*). (*C*) Contour-length histograms of N-DtpA (dark gray) and C-DtpA (light gray shading) compiled after fitting every peak in every F–D curve using the WLC model. The gray lines in *A* and *B* represent WLC curves that correspond to the mean contour length of each peak as obtained from fitting the contour-length histograms of N-DtpA and C-DtpA using a sum of Gaussian distributions (light gray and black dashed lines in *C*). The numbers next to each WLC curve represent the contour length in amino acids. Data from all six pulling velocities (160, 320, 630, 1,120, 2,230, and 4,570 nm/s) have been pooled. *n* gives the number of F–D curves used for the superimpositions in *A* and *B* and analyzed for the contour-length histograms in *C*.

Unfolding of the elongated transporter C_{long}-DtpA showed that one force-peak pattern of F–D curves shifted to longer distances but did not change its characteristic sequence of force peaks. Because this shift corresponded to the differences in the length of the C-terminal extensions of C-DtpA and C_{long}-DtpA, we could demonstrate that the predominant force-peak pattern of F–D curves corresponds to unfolding of DtpA from the terminus carrying the His-tag (*SI Appendix 4*). Next we focused on analyzing and interpreting the predominant classes of F–D curves recorded for N-DtpA and C-DtpA.

Interactions Stabilizing the Unfolding Intermediates of DtpA Depend on the Unfolding Direction. F–D curves recorded upon the unfolding of both N-DtpA and C-DtpA showed seven characteristic force peaks (Fig. 3 *A* and *B*). Each force peak from each F–D curve was fitted using the worm-like-chain (WLC) model to reveal the contour length of the unfolded and stretched transporter polypeptide (35, 45). Histograms were generated showing the contour length at which the force peaks predominantly occurred (Fig. 3*C*). To reveal the mean contour lengths of the characteristic force peaks, all peaks of each histogram were simultaneously fitted using a Gaussian mixture model (46). The contour length of a force peak described the length (in amino acids) of the already unfolded and fully stretched polypeptide. This unfolded polypeptide stretch tethered the AFM tip and the membrane-embedded unfolding intermediate of DtpA. Upon further pulling, the stretching of the unfolded polypeptide transduced the mechanical pulling force from the AFM cantilever to the unfolding intermediate until the next structural segment of the transporter unfolded. Thus, the contour length of every force peak allowed us to localize the interactions stabilizing a structural segment of the transporter (28, 44).

When DtpA was unfolded from the N-terminal end (N-DtpA), the seven characteristic force peaks occurred at mean contour lengths of 80, 109, 184, 247, 307, 403, and 484 aa. When DtpA was unfolded from the C-terminal end (C-DtpA), the seven characteristic force peaks occurred at contour lengths of 100, 170, 207, 251, 316, 391, and 450 aa (Fig. 3). The contour length of each force peak localizes an interaction stabilizing a structural segment of the peptide transporter, and the amplitude of the force peak describes the strength of the stabilizing interactions. At a pulling velocity of 640 nm/s, the mean forces required to unfold the individual structural segments of N-DtpA ranged from 38 ± 8 to 71 ± 11 pN (mean ± SD); for C-DtpA unfolding, these forces ranged from 53 ± 9 to 81 ± 22 pN (*SI Appendix 5* and Table S2). Thus the mechanical unfolding of DtpA from the C terminus required, on average, slightly more force than the unfolding from the N terminus. Such differences in the interaction strengths are expected, because the mechanical force applied directs the membrane protein along the unfolding pathway in the unfolding energy landscape (28, 29, 47). Thus, unfolding from the C- and the N-termini directs the membrane protein along different unfolding pathways. Each unfolding barrier (i.e., unfolding step of the transporter) taken along these pathways represents a unique set of stabilizing interactions.

Localizing the Interactions That Stabilize DtpA. Next we used the contour lengths obtained from fitting the contour-length histograms to localize the interactions that stabilize structural segments of DtpA (Fig. 4). To do so, we generated a secondary structure model of DtpA using the software tool TMHMM (*SI Appendix 6*) (48). The first force peak in an F–D curve records the unfolding of a stable structural segment and localizes the interactions stabilizing this structural segment. The subsequent force peaks localize the interactions stabilizing the next structural segments. We used the mean positions of the unfolding force peaks obtained from the contour-length histograms to determine the position of the stabilizing interactions in the secondary structure model.

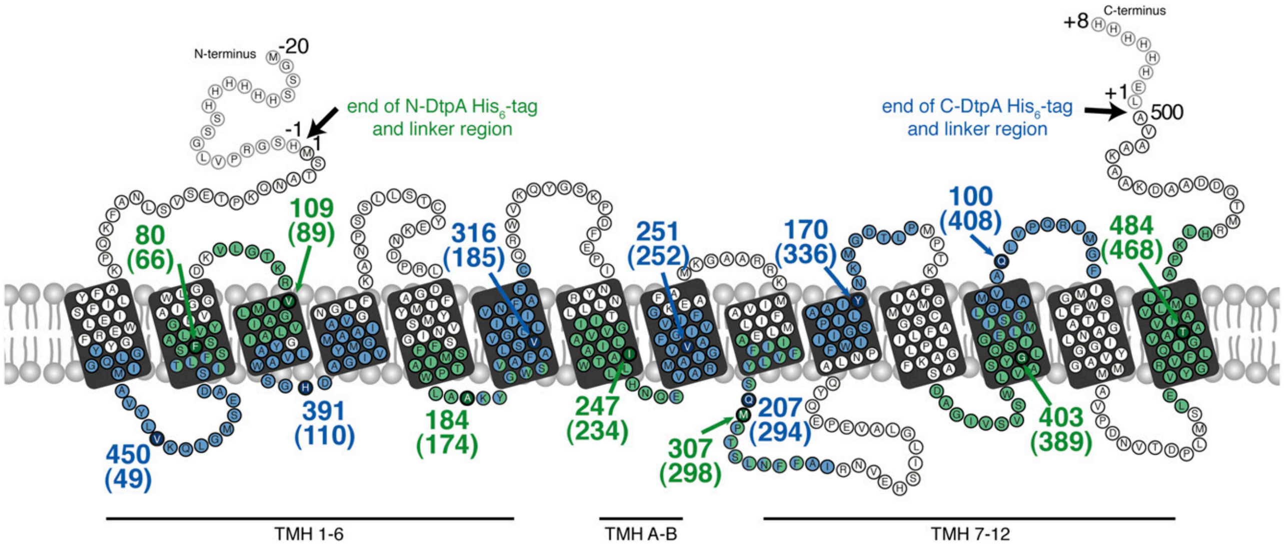

Fig. 4. Mapping the interactions stabilizing DtpA. Stabilizing interactions detected upon unfolding DtpA are mapped onto the model of the secondary structure of DtpA. The mean interactions were localized (colored arrows pointing to amino acids) using the mean contour length of force peaks (Fig. 3). The numbers at the arrows indicate the contour lengths at which the interactions primarily occur. Numbers in parentheses indicate amino acid positions in the wild-type DtpA sequence. Green and blue colors indicate interactions determined from N- and C-terminal unfolding, respectively. Light colored amino acids represent the SD of the mean contour length of the force peak detecting the stabilizing interactions. Circles with split colors indicate overlapping SD ranges for interactions detected upon unfolding DtpA from the N- and C terminus. If an interaction is located within the membrane plane or on the support-facing side of the membrane, a membrane compensation procedure was applied to estimate the position within the secondary structure (*Methods*). Light gray circles highlight the N- and C-terminal extensions. TMHs are labeled 1–12 and A–B. TMHs 1–12 correspond structurally to the TMHs observed in other MFS transporters. TMHs A–B are an insertion between the two protein domains set up by TMHs 1–6 and TMHs 7–12. The function of TMHs A–B is not yet known. In the crystal structures of homologous transporters (PepT$_{\text{So}}$ and PepT$_{\text{St}}$) these TMHs are located at the periphery of the transporter (10, 20). The secondary structure of DtpA was predicted using the TMHMM algorithm (*SI Appendix 6*) (48). In vivo, both termini are located on the cytoplasmic side of the membrane.

For N- and C-terminal unfolding, we started counting from the corresponding terminus. To obtain the correct location of the stabilizing interactions, we had to consider the length of His-tags and polypeptide linkers. If a stabilizing interaction was located on the mica-facing side of the membrane or within the lipid membrane, we applied a membrane-compensation procedure, which ensured that the thickness of the membrane was taken into account when a stabilizing interaction was localized (49, 50). After all interactions stabilizing DtpA on the putative secondary structure were mapped, it became evident that upon unfolding from the N- and C terminus the transporter was stabilized by the interactions being differently localized (Fig. 4). This different localization of stabilizing interactions has been described previously and is not surprising, because a membrane protein unfolded from different terminal ends follows different unfolding pathways (50, 51).

Inhibition of DtpA by Lys[Z-NO$_2$]-Val Affects TMH 2. Previously, we showed that the interaction of transporters with ligands or inhibitors can change the appearance of force peaks detected by SMFS (30–33). This interaction can change the amplitude and/or the frequency at which a force peak occurs. To examine which interactions and structural regions of DtpA are affected by inhibiting the peptide transport with Lys[Z-NO$_2$]-Val, we applied SMFS to characterize N-DtpA and C-DtpA in the absence and presence of 100 μM Lys[Z-NO$_2$]-Val (Fig. 5 and *SI Appendix 7*). For C-DtpA, the F–D curves recorded in the presence and absence of the inhibitor did not show significant changes (*SI Appendix*, Fig. S7). Consequently, the amplitude and the frequencies of the force peaks did not change. In the presence of 100 μM Lys[Z-NO$_2$]-Val, N-DtpA investigated by SMFS showed the same seven characteristic force peaks as observed in the absence of the inhibitor (Fig. 5*A*). Thus inhibitor binding did not alter the position or the amplitude of the force peaks in either C-DtpA or N-DtpA. In N-DtpA, however, Lys[Z-NO$_2$]-Val affected the frequency of the force peak located at a contour length of 80 aa. This effect is reflected by the significantly increased density of the force peak in the density plot of superimposed F–D curves (Fig. 5*A*). Contour-length histograms calculated after fitting every peak of every F–D curve corroborated the increased occurrence of that force peak (Fig. 5*B*). To quantify the effect, we determined the probability for all seven characteristic force peaks at six different pulling velocities independently and then calculated the average occurrence of every

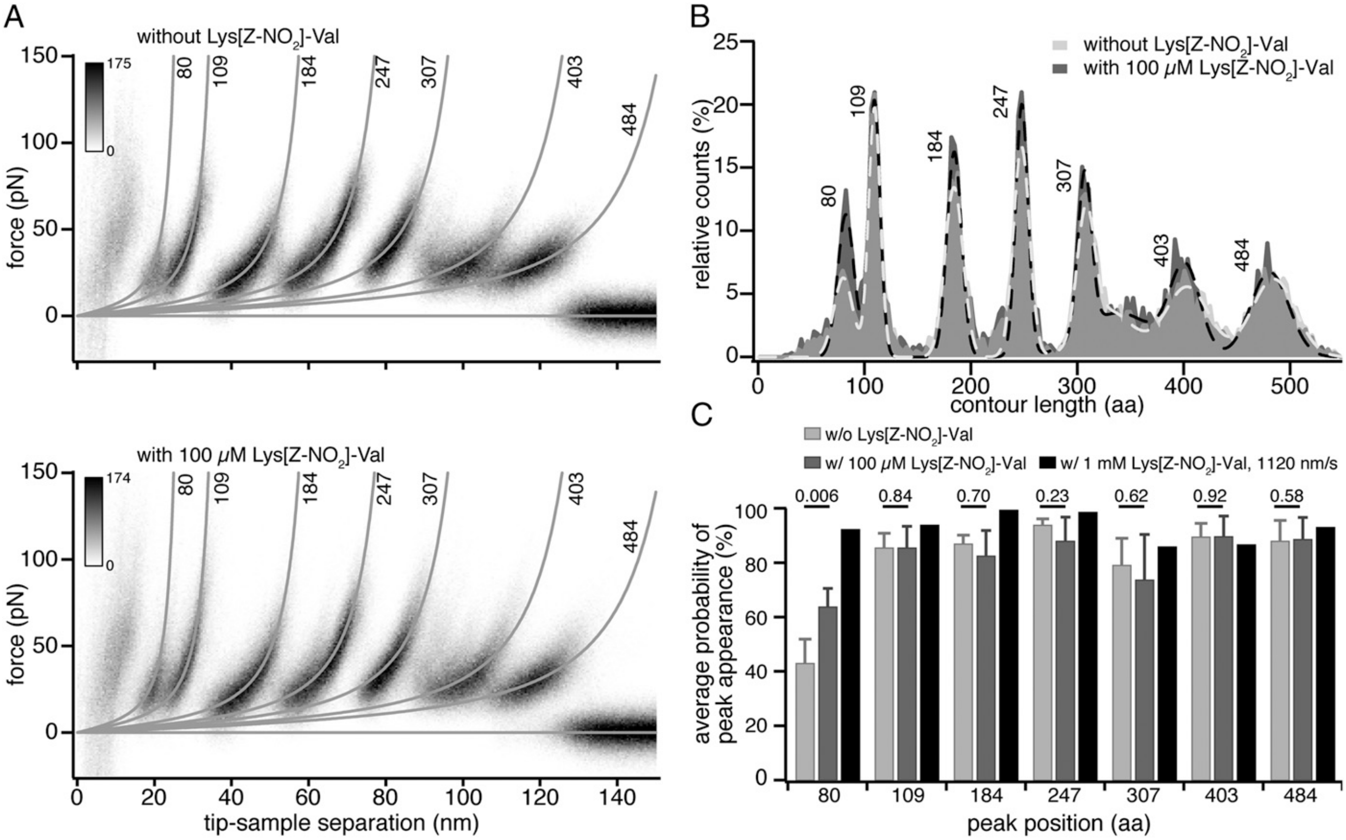

Fig. 5. Detecting the interaction of Lys[Z-NO$_2$]-Val with DtpA by SMFS. (*A*) Density plot representation of superimposed F–D curves of N-DtpA in the absence (*Upper*, $n = 584$) and presence (*Lower*, $n = 579$) of 100 μM Lys[Z-NO$_2$]-Val. Solid gray lines indicate WLC curves; contour lengths (in amino acids) are indicated at the top of each curve. (*B*) Contour-length histograms compiled after fitting all force peaks in all F–D curves recorded for the unfolding of N-DtpA in the absence (light gray, $n = 644$) and presence (dark gray, $n = 644$) of 100 μM Lys[Z-NO$_2$]-Val. Light and dark gray dashed lines represent the envelope of the sum of the Gaussian distribution function fitted to the histograms. Numbers next to each peak give the average contour length obtained from the sum of Gaussian fit. (*C*) Probability of peak appearance (± SD) of the seven characteristic force peaks detected in each F–D curve. For N-DtpA in the absence (light gray bars) and presence of 100 μM Lys[Z-NO$_2$]-Val (dark gray bars), the probability of force peak appearance was calculated separately at each of the six pulling speeds (160, 320, 640, 1,120, 2,230, and 4,570 nm/s) used to unfold N-DtpA and was integrated. Black bars represent the probability of peak appearance in presence of 1 mM Lys[Z-NO$_2$]-Val at a pulling velocity of 1,120 nm/s ($n = 126$). Values given above the columns represent the *P* values obtained from Mann–Whitney–Wilcoxon rank tests. For superimpositions and contour-length histograms, data from the six pulling speeds were pooled. *n* gives the number of F–D curves superimposed (*A*) and analyzed (*B* and *C*). Experiments were performed in buffer solution [10 mM Tris·HCl (pH 7.4), 150 mM NaCl] at room temperature and at the inhibitor concentration indicated.

force peak (Fig. 5*C*). The probability of occurrence was increased significantly only for the force peak detected at a contour length of 80 aa, which shifted from 43 ± 9% (mean ± SD) in absence of Lys[Z-NO_2]-Val to 64 ± 7% in presence of 100 μM Lys[Z-NO_2]-Val (P = 0.006). To see whether this effect depends on the concentration of the inhibitor, we also unfolded N-DtpA in the presence of 1 mM Lys[Z-NO_2]-Val (*SI Appendix 7* and Fig. S8). At this fully saturated inhibitor concentration (Fig. 1), the probability of detecting the force peak at 80 aa reached 92% (Fig. 5*C*).

Discussion

Lys[Z-NO_2]-Val Is a High-Affinity Inhibitor of DtpA. DtpA shows a substrate specificity very similar to that of hPEPT1 (4). For example, the antibacterial compound alafosfalin and the cancer therapeutic compound 5-aminolevulinic acid show similar affinities for the human hPEPT1 and the bacterial DtpA (4, 42). Both transporters also mediate uptake of the same subset of β-lactam antibiotics (3). Furthermore, both transporters share a sequence identity and similarity of 24% and 29%, respectively (*SI Appendix 6*). Therefore we investigated whether the inhibitor Lys[Z-NO_2]-Val, which shows the highest affinity to hPEPT1, also inhibits DtpA. Our in vivo uptake experiments using *E. coli* overexpressing DtpA revealed an inhibitory constant of 43 μM. In comparison, in vivo uptake experiments using *Pichia pastoris* expressing rabbit PEPT1 and a human colon carcinoma cell line (Caco-2) expressing hPEPT1 revealed a K_i of 2 μM for Lys[Z-NO_2]-Val (41). Thus, Lys[Z-NO_2]-Val displays an ∼20-fold lower affinity for DtpA than for hPEPT1. The structurally related compound Lys[Z-NO_2]-Pro also shows an approximately fourfold reduced affinity to DtpA as compared with hPEPT1, with K_is of 30 and 7 μM, respectively (4, 41). Although the affinity was lower for Lys[Z-NO_2]-Val than for Lys[Z-NO_2]-Pro, they show the same trend and remain the two strongest inhibitors for DtpA known to date.

Inter- and Intramolecular Interactions Stabilize Certain Structural Regions of DtpA. To localize structurally the interactions stabilizing DtpA in the absence and the presence of the inhibitor, we conducted SMFS. The F–D curves recorded revealed reproducible patterns of force peaks, indicating that the interactions stabilizing DtpA against unfolding were established in a highly reproducible manner. Each force peak of this pattern describes the unfolding of a structural segment stabilizing DtpA. The amplitude of the force peak describes the strength of the stabilizing interactions, and the contour length of this force peak allows the interaction to be localized structurally. Therefore we generated a secondary structure model of DtpA (Fig. 4 and *SI Appendix 6*). To judge the quality of the secondary structure prediction, we aligned the sequences of DtpA with those of $PepT_{So}$, and $PepT_{St}$ whose crystal structures have been solved. The prediction fits the secondary structures of $PepT_{So}$ and $PepT_{St}$ remarkably well (*SI Appendix 6*). Using the mean contour lengths of the force peaks recorded from N-DtpA and C-DtpA (*SI Appendix*, Table S2), we mapped the stabilizing interactions to the predicted secondary structure of DtpA (Fig. 4). In both cases the stabilizing interactions are located at or close to one end of a TMH (Fig. 4). However, these interactions sometimes stabilized regions in the middle of a TMH or of a polypeptide loop. A comparison of the locations of the stabilizing interactions established in N- and C-terminally unfolded DtpA shows that their precise location depends on the direction of unfolding. This behavior is expected, because the interaction forces detected by SMFS represent the sum of inter- and intramolecular interactions, which depend on the direction of the applied mechanical force (44, 52–54).

Inhibitor Binding Stabilizes the Functionally Important TMH 2. Unfolding of DtpA in the presence of 100 μM and 1 mM Lys[Z-NO_2]-Val significantly increased the probability of detecting the force peak at a contour length of 80 aa (Fig. 5*C*). This force peak locates the interactions that stabilize TMH 2. Force peaks detected at all other positions remained virtually unaffected by inhibitor binding (Fig. 5*C* and *SI Appendix 7*).

TMH 2 is one of the most interesting structural segments in peptide transporters of the PTR family. Early studies suggested that TMHs 1–4 and TMHs 7–9 are important for transport activity and are involved in forming the ligand-binding site (55–58). Notably, the recently obtained crystal structures revealed that TMH 2 packs closely with TMH 1, TMH 7, and TMH 8 in the inward-facing conformational state when the closed extracellular gate seals the ligand-binding site from the extracellular space (*SI Appendix 6*) (10, 20–22). A comparison of the crystal structures of the inward-facing occluded $PepT_{So}$ with the inward-open conformational states of $PepT_{St}$ and the *E. coli* lactose permease LacY reveals that, during the opening of the intracellular gate, TMH 10 and TMH 11 bend at defined pivot points, and TMH 7 displaces toward TMH 2 (10, 20, 59). These structural changes include a localized movement of the extracellular end of TMH 11, which packs TMH 2 and TMH 7 more closely. TMH 7 itself is stabilized through conserved salt-bridge interactions with TMH 1. Overall, these rearrangements observed between the occluded inward-facing conformational state of $PepT_{So}$ and the inward-open conformational state of $PepT_{St}$ strengthen the interactions of TMH 2 with its surroundings to close the extracellular gate. Like $PepT_{So}$, the crystal structure of EmrD in the occluded conformational state shows tight interactions between the extracellular ends of TMH 2 and TMH 7 that block access to the ligand-binding pocket (60). Complementarily, the crystal structure of the *E. coli* fucose transporter FucP in the outward-open conformational state exhibits a large cavity on the extracellular surface that is thought to be the entry route of fucose to the ligand-binding site (61). In the case of FucP, little interaction is observed between TMH 2 of the N-terminal six-helix bundle and TMH 7 and TMH 11 on the C-terminal bundle. Kaback and coworkers (62, 63) could identify the interface between TMH 2 and TMH 7 to establish the extracellular gate in LacY using chemical cross-linking and cysteine-labeling assays. Furthermore, a comparison of the crystal structures of $PepT_{So}$ in the occluded inward-facing conformational state (10) with LacY in the inward-open conformational state (59) suggests that the region around the functionally important H61 in $PepT_{So}$ (S64 in DtpA), which is located at the bottom of the ligand-binding pocket, undergoes large conformational changes when switching between the occluded inward-facing and inward-open conformational states. Although in $PepT_{So}$ H61 is completely buried in the interface between TMH 2 and TMH 7, the corresponding residue in LacY is fully exposed to the interior of the ligand-binding pocket (10, 59). In summary, conformational changes taking place during closure of the extracellular gate lead to stabilization of the extracellular half of TMH 2.

Inhibitor Binding Shifts the Equilibrium Between Two Conformational States. The presence of 100 μM or 1 mM of Lys[Z-NO_2]-Val increases the frequency of detecting the force peak at 80 aa that characterizes the stability of TMH 2 of DtpA. In the model of the secondary structure, the stabilizing interaction characterized by this force peak is centered at F66 and extends to I60 and G72. Three functionally important residues (F63, S64, and Y71) (*SI Appendix 6*) lie very close to the stabilizing interaction detected by the force peak at 80 aa. This force peak detecting the stability of TMH 2 also was detected in the absence of the inhibitor. However, binding of the inhibitor clearly increased the frequency of detecting a stabilized TMH 2 but did not change the strength of the interactions stabilizing TMH 2 (*SI Appendix*, Fig. S9). Thus, we propose that inhibitor binding alters the conformational equilibrium of DtpA: In the absence of inhibitor, DtpA can interconvert dynamically between two conformational states that differ in whether additional interactions stabilize TMH 2 (force peak at 80 aa). In the absence of inhibitor, the conformation showing a stabilized TMH 2 is slightly less prevalent (~43% vs. ~57%). Upon inhibitor binding, DtpA assumes the conformation stabilizing TMH 2. As the concentration of the inhibitor increases, the probability that DtpA will have the conformation characterized by a stabilized TMH 2 increases, reaching ~92% at saturation (Fig. 5*C*).

The SMFS data suggest that the presence or absence of the force peak at 80 aa can be attributed to two different conformations of TMH 2 within DtpA. It may be speculated that these two conformations reflect the inward- and outward-facing conformational states of the transporter (Fig. 6). The frequency with which these two conformations occur depends on inhibitor binding and hence on the concentration of the inhibitor. Thus, it is reasonable to assume that, from the perspective of an energy landscape describing the two conformational states of the transporter, the two states populate different energy wells (Fig. 6) (47). Binding of the inhibitor stabilizes the inhibited (i.e., inward-facing) conformational state and consequently shifts the conformational equilibrium.

Conclusions

We applied SMFS to quantify and localize the interactions stabilizing the peptide transporter DtpA and to characterize to which extent these interactions change upon binding of the strong inhibitor Lys[Z-NO_2]-Val. In the unbound state DtpA resides in or dynamically interconverts between two conformations, which differ mainly in whether TMH 2 is stabilized. In the unbound state ~43% of all DtpA molecules adopted the conformation showing a stabilized TMH 2, and ~57% of DtpA molecules adopted a conformation showing no particular stabilization of TMH 2. Inhibitor binding significantly affected the interactions stabilizing TMH 2, and the probability of detecting the stabilized TMH 2 increased as the concentration of the inhibitor increased, reaching ~92% at saturation. This result shows nicely how inhibitor binding shifts the populations of DtpA conformational states. One may speculate whether the two DtpA conformations observed reflect the so-called inward- and outward-facing conformations that describe alternate conformational states of the transporter during substrate translocation (64, 65). In the inhibitor-bound state, DtpA preferably resides in one conformational state, which is characterized by interactions stabilizing the extracellular half of TMH 2. The crystal structures of DtpA homologs in the inward-open and occluded inward-facing conformational states indicate that the closure of the extracellular gate to the ligand-binding pocket requires structural rearrangements in the vicinity of TMH 2 and interactions of TMH 2 with other TMHs. Therefore, the inward-facing conformational state may be characterized by a stabilized TMH 2 representing the Lys[Z-NO_2]-Val–inhibited state.

The alternating-access model of membrane transporters is widely supported by biochemical bulk studies (64–66). During the past decade, atomic models obtained by X-ray crystallography have contributed significantly to the understanding of the alternating-access mechanism of MFS transporters. However, it is noteworthy that 3D crystals are commonly grown from membrane proteins under nonnative conditions; i.e., membrane proteins are detergent-solubilized and crystallized, preferably in one conformation. In marked contrast to X-ray crystallography, SMFS characterizes transporters that are embedded in the lipid membrane and are exposed to buffer solution and to ambient temperatures. In this respect, SMFS provides insight into the dynamic nature of the conformations that single-peptide transporters assume in the absence and presence of inhibitors. The quickly progressing SMFS methodology soon will allow the interaction forces of membrane proteins to be detected with much improved sensitivity (~1 pN) and spatial accuracy (~0.1 nm) and with significantly improved statistics (67, 68). In the future these advances may provide much more detailed information about the interactions that stabilize coexisting conformational substates of membrane proteins residing in their physiologically relevant environment.

Methods

Materials. Unless stated otherwise, all chemicals were of analytical grade and were purchased from Sigma-Aldrich. All buffers were prepared using nanopure water (18 MΩ/cm). Lys[Z-NO_2]-Val was synthesized as described previously (41).

Cloning of the DtpA Versions C-DtpA, C_{long}-DtpA and N-DtpA. To obtain C-DtpA, the *DtpA* gene was cloned as described previously into a modified version of the pET-21 vector resulting in the construct pET-21b-rbs-T7-DtpA-His (4). This cloned DtpA version had the C-terminal amino acid extension LEHHHHHH. To generate C_{long}-DtpA, a point mutation was first introduced into pET-21b-rbs-T7-DtpA-His (C-DtpA) after the STOP codon to generate

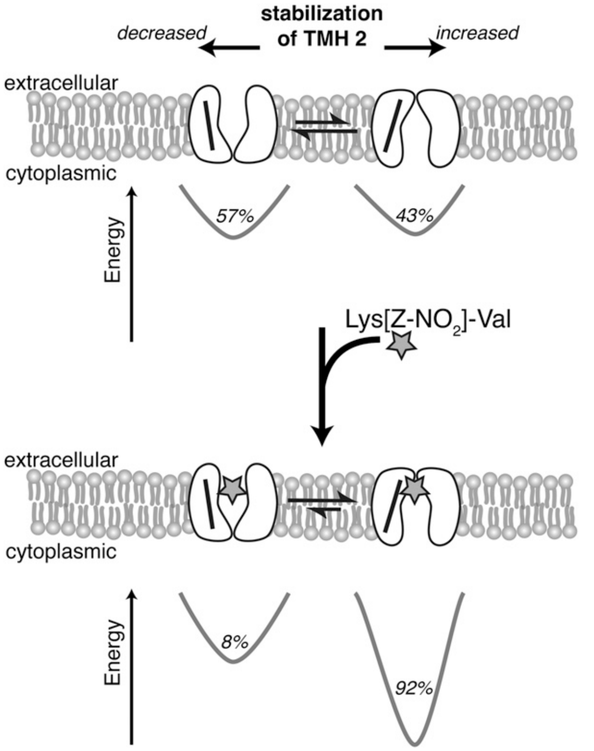

Fig. 6. Model of the inhibitor changing the stability of TMH 2 and the conformational state of DtpA. According to the alternate-access model for membrane-embedded transporters (64–66), the ligand-binding site of a transporter is sequentially accessible from the extracellular and the cytoplasmic side of the cell membrane. Thus, the transporter adopts outward-facing and inward-facing conformational states (shown on the left and right sides of the cartoon, respectively). In this model we speculated that the inward-facing conformational state is stabilized by TMH 2, because additional interactions between TMH 2 with its surroundings are required for closure of the extracellular gate (20). Our SMFS measurements quantified that unliganded DtpA coexists in two conformations that differ depending on whether the stability of TMH 2 is enhanced. The probability of detecting DtpA residing in the outward-facing conformation characterized by the less stable TMH 2 is ~57%, and the probability of detecting DtpA residing in the inward-facing conformation characterized by a stable TMH 2 is ~43%. Thus, from the perspective of an energy landscape, the outward-facing conformational state resides in a lower energy well as compared with the inward-facing conformational state. Unliganded DtpA can interconvert dynamically between the inward- and outward-facing conformations. Inhibitor (Lys[Z-NO_2]-Val, indicated by stars) binding stabilizes TMH 2 and shifts the probability of detecting a stabilized TMH 2 to ~92%. Accordingly, inhibitor binding lowers the energy well stabilizing the DtpA conformation stabilized by TMH 2.

a SacI restriction site using the forward primer 5′-CAC CAC CAC CAC TGA GCT CCG GCT GCT AAC-3′ and the reverse primer 5′-GTT AGC AGC CGG AGC TCA GTG GTG GTG GTG-3′ and the QuikChange Site-Directed Mutagenesis Kit (Stratagene). Next, the construct was digested with HindIII and SacI to remove the *DtpA* gene and the C-terminal extension. The two prehybridized complementary oligonucleotide fragments, which have HindIII- and SacI-compatible ends, then were inserted into the vector: Upper, 5′ (HindIII) AGC TTG CGG CCG CAC TCG AGC TGG AAG TTC TGT TCC AGG GGC CCG TCG ACC ATC ACC ACC ATC ATC ACC ATC ACC ACC ACT GAG CT (SacI) 5′ and Lower, 3′ (HindIII) CAG TGG TGG TGA TGG TGA TGA TGG TGG TGA TGG TCG ACG GGC CCC TGG AAC AGA ACT TCC AGC TCG AGT GCG GCC GCA (SacI) 5′. Reinsertion of the *DtpA* gene using the HindIII and XhoI restriction sites into this new vector (pZUDF21-rbs-3C-10His) resulted in a DtpA version (C_{long}-DtpA) with the C-terminal amino acid extension LELEVLFQGPVDHHHHHHHHHH. The N-DtpA version was created by cloning the *DtpA* gene from the carrier construct pET-21b-rbs-T7-DtpA-His into the pET-15b vector using the restriction enzymes NdeI and BamHI, and the forward primer 5′-CCA AAA CAT ATG TCC ACT GCA AAC CAA AAA CC-3′ and the reverse primer 5′-CCA AAA GGA TCC TCA CGC TAC GGC TGC TTT CGC CGC-3′. This cloned DtpA version had the N-terminal amino acid extension MGSSHHHHHHSSGLVPRGSH.

Overexpression, Purification, and Reconstitution of C-DtpA, C_{long}-DtpA, and N-DtpA into Proteoliposomes. Overexpression was carried out with freshly transformed *E. coli* BL21(DE3)pLysS cells harboring the plasmids encoding C-DtpA, C_{long}-DtpA, or N-DtpA. Cultures were grown in lysogeny broth (LB) medium supplemented with 0.1 mg/mL ampicillin at 37 °C in an orbital shaker. Expression of the different DtpA versions was induced at an OD_{600} of 0.6 with 0.1 mM isopropyl-β-D-thiogalactopyranoside (IPTG) for 3 h. Cells then were harvested by centrifugation (7,200 × *g*; 25 min; 4 °C), resuspended in 20 mM Tris·HCl (pH 8), 450 mM NaCl, DNase I from bovine pancreas (Sigma; 400 μg for cells from 12 L of culture), and lysed by four passages through a microfluidizer (M-110P; Microfluidics Corp) at 16,000 psi. Unbroken cells were removed by centrifugation (12,000 × *g*; 10 min; 4 °C). Membranes were collected from the supernatant by ultracentrifugation (150,000 × *g*; 1 h; 4 °C), homogenized in 20 mM Tris·HCl (pH 8), 450 mM NaCl, and ultracentrifuged. This membrane-washing procedure was repeated once. Pellets then were homogenized and resuspended in the same buffer, aliquoted into 2- to 3-mL fractions (corresponding to membranes from 2 L of LB medium), flash frozen in liquid nitrogen, and stored at −80 °C until use.

For purification, one aliquot of membrane suspension was solubilized for 2 h at 4 °C under gentle agitation in 2% (wt/vol) *N*-dodecyl-β-D-maltopyranoside (Affymetrix; V_{tot} = 7 mL) in Buffer S [20 mM Tris·HCl (pH 8), 300 mM NaCl, 250 mM betaine, 10% (vol/vol) glycerol, 0.01% NaN_3]. After ultracentrifugation (100,000 × *g*; 1 h; 4 °C), the supernatant was diluted twofold with 5 mM histidine in Buffer S and incubated with 0.5 mL preequilibrated Ni-NTA Superflow beads (Qiagen) for 2 h at 4 °C on a rotational shaker. The beads then were transferred into a column and washed with 21 mL of 5 mM L-histidine, 0.04% *N*-dodecyl-β-D-maltopyranoside in Buffer S. DtpA was eluted from the Ni-NTA beads with 400 mM imidazole in Buffer S. For C-DtpA, C_{long}-DtpA and N-DtpA, the yields were between 0.6–1.2 mg of pure protein per 2 L of cell culture.

For reconstitution into proteoliposomes, purified DtpA versions were mixed with DMPC (Avanti Polar Lipids Inc.) solubilized in *N*-decyl-β-D-maltopyranoside [stock solution: 5 mg/mL DMPC, 1% *N*-decyl-β-D-maltopyranoside, 20 mM Tris·HCl (pH 8), 150 mM NaCl, 10% (vol/vol) glycerol, 0.01% NaN_3] (Affymetrix) to achieve lipid:protein ratios of 0.85 and 0.9 (wt/wt). The final protein concentration of each DtpA version after the addition of lipids was adjusted to ∼1 mg/mL. To promote reconstitution of DtpA into proteoliposomes, samples were dialyzed against detergent-free buffer [20 mM Tris·HCl (pH 8), 150 mM NaCl, 250 mM betaine, 10% (vol/vol) glycerol, 0.01% NaN_3] for 1 wk at room temperature.

In Vivo Peptide Uptake Assay. *E. coli* BL21(DE3)pLysS cells were transformed with the C_{long}-DtpA vector pZUDF21-rbs-DtpA-3C-10His or with the empty vector as a control. Cells were grown to an OD_{600} of 0.8, and protein expression was induced by addition of 0.1 mM IPTG. After 3-h induction time, OD_{600} was measured, and a volume corresponding to the cell amount of 1 mL at OD_{600} 15 was pelleted (5,000 × *g*; 15 min; 4 °C) and resuspended in 2 mL of cold uptake buffer [50 mM Hepes-NaOH (pH 7.5), 150 mM NaCl, 5 mM glucose]. Then 30 μL of cold cell suspension was added to a reaction vial containing 10 μL with 0.2 μCi [^{3}H]-Ala-Ala (0.074 Ci/mmol) (Moravek Biochemicals) and 10 μL of a 5× stock of Lys[Z-NO_2]-Val (0, 0.0023, 0.0077, 0.025, 0.083, 0.28, 0.91, 3 mM end concentration in 50 μL) and was incubated for 1.5 min at room temperature. Uptake was stopped by the addition of 450 μL cold uptake buffer followed by centrifugation (15,000 × *g*; 1 min; 4 °C). The pellet was resuspended in 50 μL 5% (wt/vol) SDS, transferred to a white 96-well plate, and mixed with 150 μL Microscint-40 liquid scintillation mixture (PerkinElmer). The signal was read in a Topcount scintillation counter (PerkinElmer). Data were analyzed using the "one site – Fit K_i" equation in Prism5 (Graphpad software) with a K_d of Ala–Ala for DtpA set to 470 μM (4) and Ala–Ala concentration at 54 μM. For each data point the respective background uptake of control cells was subtracted.

AFM Imaging. Proteoliposomes (0.3 μL) containing ∼1 mg/mL of the corresponding DtpA version were adsorbed in 30 μL SMFS buffer [10 mM Tris·HCl (pH 7.4), 150 mM NaCl] on freshly cleaved mica for 25 min (43). After adsorption, the buffer was exchanged several times to remove loosely bound membranes. Contact-mode AFM imaging was performed using a Nanoscope III Multimode AFM (Bruker) in buffer solution. The liquid cell was equipped with soft cantilevers (Bruker SNL, 200 μm length, nominal k = 0.06 N/m; Bruker). During AFM imaging, contact forces applied to the AFM cantilever tip were minimized (<100 pN), and gains were optimized to minimize the signal error.

SMFS. SMFS was conducted at 25 °C in buffer solution using a Nanowizard II Ultra AFM (JPK Instruments) equipped with BioLevers (60-μm length, nominal k = 0.03 N/m) (Olympus). Before adsorption, 0.5 μL of DtpA proteoliposomes (∼1 mg/mL DtpA) were mixed with 20 μL SMFS buffer and were incubated for 10 min at 4 °C. For experiments in the presence of inhibitor, the buffer was supplemented with 100 μM or 1 mM Lys[Z-NO_2]-Val. Proteoliposomes in SMFS buffer were adsorbed to freshly cleaved mica for 20 min. The buffer was exchanged several times to remove loosely bound membranes and debris. Membrane patches containing DtpA were located by contact-mode AFM imaging. Eventually, proteoliposomes or double-layered membrane patches were dissected by the scanning AFM tip (69) to yield single-layered membrane patches of densely packed DtpA for SMFS.

DtpA was unspecifically attached to the AFM tip by pushing the tip onto the membrane with a force of ∼1 nN for 0.5–1 s. Subsequently, the cantilever was retracted from the membrane at different velocities (160, 320, 640, 1,120, 2,230, and 4,570 nm/s), and the cantilever deflection and the distance between tip and membrane surface were recorded. The interaction force at each distance was calculated from the cantilever deflection using Hook's law, which resulted in F–D curves. Before each experiment the spring constant of each cantilever was estimated using the equipartition theorem (70).

SMFS Data Selection and Analysis. In contrast to the unfolding of soluble proteins, in which the last force peak of an F–D curve corresponds to detachment of the peptide from either the cantilever tip or the support, the last force peak in the unfolding of membrane proteins denotes the unfolding of the last stable structural segment that remained anchored in the lipid bilayer (49, 51). When the stability of this last segment has been overcome, the membrane protein has been unfolded completely, and the entire polypeptide is extracted from the lipid membrane. This unique unfolding behavior can be used as criterion to select F–D curves that are sufficiently long to describe the complete unfolding of a membrane protein (49). As selection criteria, we assumed for DtpA that either TMH 11 and TMH 12 together or TMH 12 alone established the last structural segment to be unfolded. Based on the prediction of the secondary structure and sequence alignment to transporters of known topology (*SI Appendix 6*), we expected the last force peak to appear at a contour length (L_c) of 400–490 aa. Therefore, we selected F–D curves for analysis that showed an overall distance of 110–140 nm (assuming that one amino acid is ∼0.36 nm long). The selected F–D curves were superimposed, and every force peak of each F–D curve was fitted with the WLC model (45) using a persistence length of 0.4 nm and a monomer length of 0.36 nm per amino acid (71). Contour lengths and rupture forces were analyzed statistically, and contour-length histograms were created. Peaks in these histograms were simultaneously fitted using a sum of Gaussian distributions (46). This procedure revealed the mean contour lengths of the unfolded and stretched polypeptides of DtpA and indicated the border positions of the stable structural segments that were mapped on the secondary structure of DtpA. Membrane compensation was applied for borders that occurred on the support-facing side of the membrane or within the membrane plane (49, 50). Force histograms were compiled for each force peak determined from contour-length histograms. Additionally, the probability of occurrence was calculated for each force peak. Data visualization, statistical analysis, and calculations were performed using custom and built-in procedures for IgorPro 6 (Wavemetrics).

ACKNOWLEDGMENTS. We thank J. Tittel for support with data acquisition. This work was supported by the Deutsche Forschungsgemeinschaft, Grant 09-EuroSYNBIO-FP-012 NANOCELL from the European Science Foundation, the Swiss National Science Foundation, the University of Bern, and the National Centre of Competence in Research TransCure.

1. Steiner H-Y, Naider F, Becker JM (1995) The PTR family: A new group of peptide transporters. *Mol Microbiol* 16(5):825–834.
2. Daniel H, Spanier B, Kottra G, Weitz D (2006) From bacteria to man: Archaic proton-dependent peptide transporters at work. *Physiology (Bethesda)* 21(2):93–102.
3. Harder D, et al. (2008) DtpB (YhiP) and DtpA (TppB, YdgR) are prototypical proton-dependent peptide transporters of *Escherichia coli*. *FEBS J* 275(13):3290–3298.
4. Weitz D, et al. (2007) Functional and structural characterization of a prokaryotic peptide transporter with features similar to mammalian PEPT1. *J Biol Chem* 282(5): 2832–2839.
5. Hagting A, Kunji ERS, Leenhouts KJ, Poolman B, Konings WN (1994) The di- and tri-peptide transport protein of *Lactococcus lactis*. A new type of bacterial peptide transporter. *J Biol Chem* 269(15):11391–11399.
6. Nakajima H, Hagting A, Kunji ERS, Poolman B, Konings WN (1997) Cloning and functional expression in *Escherichia coli* of the gene encoding the di- and tripeptide transport protein of *Lactobacillus helveticus*. *Appl Environ Microbiol* 63(6):2213–2217.
7. Perry JR, Basrai MA, Steiner HY, Naider F, Becker JM (1994) Isolation and characterization of a *Saccharomyces cerevisiae* peptide transport gene. *Mol Cell Biol* 14(1): 104–115.
8. Biegel A, et al. (2006) The renal type H$^+$/peptide symporter PEPT2: Structure-affinity relationships. *Amino Acids* 31(2):137–156.
9. Daniel H, Kottra G (2004) The proton oligopeptide cotransporter family SLC15 in physiology and pharmacology. *Pflugers Arch* 447(5):610–618.
10. Newstead S, et al. (2011) Crystal structure of a prokaryotic homologue of the mammalian oligopeptide-proton symporters, PepT1 and PepT2. *EMBO J* 30(2):417–426.
11. Ernst HA, et al. (2009) Ligand binding analyses of the putative peptide transporter YjdL from *E. coli* display a significant selectivity towards dipeptides. *Biochem Biophys Res Commun* 389(1):112–116.
12. Meredith D (2009) The mammalian proton-coupled peptide cotransporter PepT1: Sitting on the transporter-channel fence? *Philos Trans R Soc Lond B Biol Sci* 364(1514): 203–207.
13. Rubio-Aliaga I, Daniel H (2002) Mammalian peptide transporters as targets for drug delivery. *Trends Pharmacol Sci* 23(9):434–440.
14. Brandsch M (2009) Transport of drugs by proton-coupled peptide transporters: Pearls and pitfalls. *Expert Opin Drug Metab Toxicol* 5(8):887–905.
15. Paulsen IT, Skurray RA (1994) The POT family of transport proteins. *Trends Biochem Sci* 19(10):404.
16. Hauser M, Kauffman S, Naider F, Becker JM (2005) Substrate preference is altered by mutations in the fifth transmembrane domain of Ptr2p, the di/tri-peptide transporter of *Saccharomyces cerevisiae*. *Mol Membr Biol* 22(3):215–227.
17. Yeung AK, et al. (1998) Molecular identification of a role for tyrosine 167 in the function of the human intestinal proton-coupled dipeptide transporter (hPepT1). *Biochem Biophys Res Commun* 250(1):103–107.
18. Hagting A, vd Velde J, Poolman B, Konings WN (1997) Membrane topology of the di- and tripeptide transport protein of *Lactococcus lactis*. *Biochemistry* 36(22):6777–6785.
19. Covitz K-MY, Amidon GL, Sadée W (1998) Membrane topology of the human dipeptide transporter, hPEPT1, determined by epitope insertions. *Biochemistry* 37(43): 15214–15221.
20. Solcan N, et al. (2012) Alternating access mechanism in the POT family of oligopeptide transporters. *EMBO J* 31(16):3411–3421.
21. Doki S, et al. (2013) Structural basis for dynamic mechanism of proton-coupled symport by the peptide transporter POT. *Proc Natl Acad Sci USA* 110(28):11343–11348.
22. Guettou F, et al. (2013) Structural insights into substrate recognition in proton-dependent oligopeptide transporters. *EMBO Rep* 14(9):804–810.
23. Malle E, et al. (2011) Random mutagenesis of the prokaryotic peptide transporter YdgR identifies potential periplasmic gating residues. *J Biol Chem* 286(26):23121–23131.
24. Jensen JM, et al. (2012) Functional investigation of conserved membrane-embedded glutamate residues in the proton-coupled peptide transporter YjdL. *Protein Pept Lett* 19(3):282–287.
25. Jensen JM, Ismat F, Szakonyi G, Rahman M, Mirza O (2012) Probing the putative active site of YjdL: An unusual proton-coupled oligopeptide transporter from *E. coli*. *PLoS ONE* 7(10):e47780.
26. Jensen JM, et al. (2012) Biophysical characterization of the proton-coupled oligopeptide transporter YjdL. *Peptides* 38(1):89–93.
27. Casagrande F, et al. (2009) Projection structure of DtpD (YbgH), a prokaryotic member of the peptide transporter family. *J Mol Biol* 394(4):708–717.
28. Kedrov A, Janovjak H, Sapra KT, Müller DJ (2007) Deciphering molecular interactions of native membrane proteins by single-molecule force spectroscopy. *Annu Rev Biophys Biomol Struct* 36(1):233–260.
29. Engel A, Gaub HE (2008) Structure and mechanics of membrane proteins. *Annu Rev Biochem* 77(1):127–148.
30. Kedrov A, Krieg M, Ziegler C, Kuhlbrandt W, Muller DJ (2005) Locating ligand binding and activation of a single antiporter. *EMBO Rep* 6(7):668–674.
31. Kedrov A, Ziegler C, Muller DJ (2006) Differentiating ligand and inhibitor interactions of a single antiporter. *J Mol Biol* 362(5):925–932.
32. Kedrov A, et al. (2010) Probing the interactions of carboxy-atractyloside and atractyloside with the yeast mitochondrial ADP/ATP carrier. *Structure* 18(1):39–46.
33. Ge L, Perez C, Waclawska I, Ziegler C, Muller DJ (2011) Locating an extracellular K$^+$-dependent interaction site that modulates betaine-binding of the Na$^+$-coupled betaine symporter BetP. *Proc Natl Acad Sci USA* 108(43):E890–E898.
34. Zocher M, Fung JJ, Kobilka BK, Müller DJ (2012) Ligand-specific interactions modulate kinetic, energetic, and mechanical properties of the human β_2 adrenergic receptor. *Structure* 20(8):1391–1402.
35. Cisneros DA, et al. (2008) Transducer binding establishes localized interactions to tune sensory rhodopsin II. *Structure* 16(8):1206–1213.
36. Sapra KT, Balasubramanian GP, Labudde D, Bowie JU, Muller DJ (2008) Point mutations in membrane proteins reshape energy landscape and populate different unfolding pathways. *J Mol Biol* 376(4):1076–1090.
37. Sapra KT, Doehner J, Renugopalakrishnan V, Padrós E, Muller DJ (2008) Role of extracellular glutamic acids in the stability and energy landscape of bacteriorhodopsin. *Biophys J* 95(7):3407–3418.
38. Kawamura S, Colozo AT, Ge L, Müller DJ, Park PS (2012) Structural, energetic, and mechanical perturbations in rhodopsin mutant that causes congenital stationary night blindness. *J Biol Chem* 287(26):21826–21835.
39. Sapra KT, Besir H, Oesterhelt D, Muller DJ (2006) Characterizing molecular interactions in different bacteriorhodopsin assemblies by single-molecule force spectroscopy. *J Mol Biol* 355(4):640–650.
40. Zocher M, Zhang C, Rasmussen SG, Kobilka BK, Müller DJ (2012) Cholesterol increases kinetic, energetic, and mechanical stability of the human β2-adrenergic receptor. *Proc Natl Acad Sci USA* 109(50):E3463–E3472.
41. Knütter I, et al. (2004) Analysis of the transport properties of side chain modified dipeptides at the mammalian peptide transporter PEPT1. *Eur J Pharm Sci* 21(1):61–67.
42. Brandsch M, Knütter I, Bosse-Doenecke E (2008) Pharmaceutical and pharmacological importance of peptide transporters. *J Pharm Pharmacol* 60(5):543–585.
43. Müller DJ, Amrein M, Engel A (1997) Adsorption of biological molecules to a solid support for scanning probe microscopy. *J Struct Biol* 119(2):172–188.
44. Bippes CA, Muller DJ (2011) High-resolution atomic force microscopy and spectroscopy of native membrane proteins. *Rep Prog Phys* 74(8):086601.
45. Bustamante C, Marko JF, Siggia ED, Smith S (1994) Entropic elasticity of lambda-phage DNA. *Science* 265(5178):1599–1600.
46. Kawamura S, et al. (2013) Kinetic, energetic, and mechanical differences between dark-state rhodopsin and opsin. *Structure* 21(3):426–437.
47. Janovjak H, Sapra KT, Kedrov A, Müller DJ (2008) From valleys to ridges: Exploring the dynamic energy landscape of single membrane proteins. *ChemPhysChem* 9(7): 954–966.
48. Melén K, Krogh A, von Heijne G (2003) Reliability measures for membrane protein topology prediction algorithms. *J Mol Biol* 327(3):735–744.
49. Müller DJ, et al. (2002) Stability of bacteriorhodopsin α-helices and loops analyzed by single-molecule force spectroscopy. *Biophys J* 83(6):3578–3588.
50. Kessler M, Gaub HE (2006) Unfolding barriers in bacteriorhodopsin probed from the cytoplasmic and the extracellular side by AFM. *Structure* 14(3):521–527.
51. Kedrov A, Ziegler C, Janovjak H, Kühlbrandt W, Müller DJ (2004) Controlled unfolding and refolding of a single sodium-proton antiporter using atomic force microscopy. *J Mol Biol* 340(5):1143–1152.
52. White SH, Wimley WC (1999) Membrane protein folding and stability: Physical principles. *Annu Rev Biophys Biomol Struct* 28(1):319–365.
53. Brockwell DJ, et al. (2003) Pulling geometry defines the mechanical resistance of a beta-sheet protein. *Nat Struct Biol* 10(9):731–737.
54. Hensen U, Müller DJ (2013) Mechanistic explanation of different unfolding behaviors observed for transmembrane and soluble beta-barrel proteins. *Structure* 21(8): 1317–1324.
55. Fei Y-J, et al. (1997) Identification of the histidyl residue obligatory for the catalytic activity of the human H+/peptide cotransporters PEPT1 and PEPT2. *Biochemistry* 36(2):452–460.
56. Döring F, et al. (1996) Functional analysis of a chimeric mammalian peptide transporter derived from the intestinal and renal isoforms. *J Physiol* 497(Pt 3):773–779.
57. Terada T, Saito H, Mukai M, Inui KI (1996) Identification of the histidine residues involved in substrate recognition by a rat H$^+$/peptide cotransporter, PEPT1. *FEBS Lett* 394(2):196–200.
58. Terada T, Saito H, Sawada K, Hashimoto Y, Inui KI (2000) N-terminal halves of rat H$^+$/peptide transporters are responsible for their substrate recognition. *Pharm Res* 17(1):15–20.
59. Abramson J, et al. (2003) Structure and mechanism of the lactose permease of Escherichia coli. *Science* 301(5633):610–615.
60. Yin Y, He X, Szewczyk P, Nguyen T, Chang G (2006) Structure of the multidrug transporter EmrD from Escherichia coli. *Science* 312(5774):741–744.
61. Dang S, et al. (2010) Structure of a fucose transporter in an outward-open conformation. *Nature* 467(7316):734–738.
62. Zhou Y, Guan L, Freites JA, Kaback HR (2008) Opening and closing of the periplasmic gate in lactose permease. *Proc Natl Acad Sci USA* 105(10):3774–3778.
63. Nie Y, Zhou Y, Kaback HR (2009) Clogging the periplasmic pathway in LacY. *Biochemistry* 48(4):738–743.
64. Guan L, Kaback HR (2006) Lessons from lactose permease. *Annu Rev Biophys Biomol Struct* 35(1):67–91.
65. Forrest LR, Kramer R, Ziegler C (2011) The structural basis of secondary active transport mechanisms. *Biochimica et Biophysica Acta (BBA) - Bioenergetics* 1807(2): 167–188.
66. Jardetzky O (1966) Simple allosteric model for membrane pumps. *Nature* 211(5052): 969–970.
67. Struckmeier J, et al. (2008) Fully automated single-molecule force spectroscopy for screening applications. *Nanotechnology* 19(38):384020.
68. Bosshart PD, et al. (2008) High-throughput single-molecule force spectroscopy for membrane proteins. *Nanotechnology* 19(38):384014.
69. Fotiadis D, et al. (2000) Surface tongue-and-groove contours on lens MIP facilitate cell-to-cell adherence. *J Mol Biol* 300(4):779–789.
70. Butt H-J, Jaschke M (1995) Calculation of thermal noise in atomic force microscopy. *Nanotechnology* 6(1):1–7.
71. Rief M, Gautel M, Oesterhelt F, Fernandez JM, Gaub HE (1997) Reversible unfolding of individual titin immunoglobulin domains by AFM. *Science* 276(5315):1109–1112.